

Article

The Family of $M^{\text{II}}_3(\text{Te}^{\text{IV}}\text{O}_3)_2(\text{OH})_2$ ($M = \text{Mg}, \text{Mn}, \text{Co}, \text{Ni}$) Compounds—Prone to Inclusion of Foreign Components into Large Hexagonal Channels

Felix Eder ¹, Matthias Weil ^{1,*}, Owen P. Missen ^{2,3}, Uwe Kolitsch ^{4,5} and Eugen Libowitzky ⁵

¹ Institut für Chemische Technologien und Analytik, Abteilung Strukturchemie, TU Wien, Getreidemarkt 9/164-E164-05, A-1060 Vienna, Austria

² School of Earth, Atmosphere and Environment, Monash University, 9 Rainforest Walk, Clayton, VIC 3800, Australia

³ Geosciences, Museums Victoria, P.O. Box 666, Melbourne 3001, Australia

⁴ Naturhistorisches Museum Wien, Burgring 7, A-1010 Vienna, Austria

⁵ Institut für Mineralogie und Kristallographie, Universität Wien, Josef-Holaubek-Platz 2, A-1090 Vienna, Austria

* Correspondence: matthias.weil@tuwien.ac.at

Abstract: $M^{\text{II}}_3(\text{Te}^{\text{IV}}\text{O}_3)_2(\text{OH})_2$ ($M = \text{Mg}, \text{Mn}, \text{Co}, \text{Ni}$) compounds crystallize isotypically in the hexagonal space group $P6_3mc$ (No. 186) with unit-cell parameters of $a \approx 13 \text{ \AA}$, $c \approx 5 \text{ \AA}$. In the crystal structure, a framework with composition $M_3(\text{TeO}_3)_2(\text{OH})_{1.5}^{0.5+}$ defines large hexagonal channels extending along [001] where the remaining OH^- anions are located. Crystal-growth studies under mild hydrothermal conditions with subsequent structure analyses on basis of X-ray diffraction methods revealed that parts of other anions present in solution such as CO_3^{2-} , SO_4^{2-} , SeO_4^{2-} , NO_3^- , Cl^- or Br^- could partly replace the OH^- anions in the channels. The incorporation of such anions into the $M_3(\text{TeO}_3)_2(\text{OH})_2$ structure was confirmed by energy-dispersive X-ray spectrometry (EDS) measurements and Raman spectroscopy of selected single-crystals.

Keywords: oxidotellurates(IV); first-row transition metals; hydrothermal synthesis; crystal chemistry; crystal structure determination; disorder



Citation: Eder, F.; Weil, M.; Missen, O.P.; Kolitsch, U.; Libowitzky, E. The Family of $M^{\text{II}}_3(\text{Te}^{\text{IV}}\text{O}_3)_2(\text{OH})_2$ ($M = \text{Mg}, \text{Mn}, \text{Co}, \text{Ni}$) Compounds—Prone to Inclusion of Foreign Components into Large Hexagonal Channels. *Crystals* **2022**, *12*, 1380. <https://doi.org/10.3390/cryst12101380>

Academic Editor: Ludmila Isaenko

Received: 31 August 2022

Accepted: 26 September 2022

Published: 28 September 2022

Publisher's Note: MDPI stays neutral with regard to jurisdictional claims in published maps and institutional affiliations.



Copyright: © 2022 by the authors. Licensee MDPI, Basel, Switzerland. This article is an open access article distributed under the terms and conditions of the Creative Commons Attribution (CC BY) license (<https://creativecommons.org/licenses/by/4.0/>).

1. Introduction

The manganese(II) oxidotellurate(VI) phase with composition $\text{Mn}^{\text{II}}_3\text{Te}^{\text{VI}}\text{O}_6$ exhibits complex magnetic behaviour. Its ambient-pressure phase is characterized by an incommensurate magnetic ordering [1,2], and its high-pressure phase by magnetic frustration [3]. The magnetic structure of the manganese(III) oxidotellurate(VI) with composition $\text{Mn}^{\text{III}}_2\text{Te}^{\text{VI}}\text{O}_6$ was established on the basis of a neutron powder diffraction study [4]. This phase gained renewed interest because it is considered a possible multiferroic [5]. On the other hand, magnetic properties of manganese(II) oxidotellurates(IV), for which numerous phases have been reported [6–11], are not well-investigated and restricted to the high-pressure polymorph $\beta\text{-Mn}^{\text{II}}\text{Te}^{\text{IV}}\text{O}_3$ [12,13]. This lack of knowledge is most probably caused by difficulties to synthesize the corresponding manganese(II) oxidotellurates(IV) as single-phases for magnetic bulk measurements or for neutron diffraction studies. With the objective to prepare different phases in the $\text{Mn}^{\text{II}}/\text{Te}^{\text{IV}}/\text{O}/(\text{H})$ system in the form of single-phase material, we started systematic studies of the phase formation in this system using solid-state or hydrothermal reactions. Although we were eventually able to grow single-crystals and to determine the crystal structures of $\alpha\text{-MnTeO}_3$, $\gamma\text{-MnTeO}_3$, $\text{Mn}_6\text{Te}_5\text{O}_{16}$, $\text{Mn}_{15}(\text{TeO}_3)_{14}(\text{OH})_2$ and $\text{Mn}_3(\text{TeO}_3)_2(\text{OH})_2$, the intended phase purity could not be achieved because all products consisted of mixtures of different phases [14].

Whereas the results of single-crystal structure analyses were inconspicuous for α -MnTeO₃, γ -MnTeO₃, Mn₆Te₅O₁₆ and Mn₁₅(TeO₃)₁₄(OH)₂ [14], those of the channel-structure of hexagonal Mn₃(TeO₃)₂(OH)₂ revealed some unsatisfactory features of the refined crystal structure model, in particular, high remaining electron densities located within the channels. Preliminary experiments indicated that the height of the remaining electron density depends on the metal salt used as the source for manganese(II) in the hydrothermal experiment, and that corresponding anions (CO₃²⁻, SO₄²⁻, SeO₄²⁻, NO₃⁻, Cl⁻, Br⁻) can be incorporated into the channels where they partly substitute the prevalent OH⁻ species. Substitution of OH⁻ by other anionic species is not uncommon and observed in several minerals, for example, apatites [15] or defernite [16], and thus of general interest.

In the current report, we present the results of partial OH⁻ substitution investigated systematically for Mn₃(TeO₃)₂(OH)₂ and, to a certain extent, for the other isotopic members of the M^{II}₃(TeO₃)₂(OH)₂ family of compounds (M = Mg, Co, Ni).

2. Materials and Methods

2.1. Synthesis

The crystal-growth procedures for all batches were conducted under hydrothermal conditions using Teflon containers with an inner volume of *ca.* 3 mL. The corresponding educt mixture, consisting of commercially available chemicals, was placed inside the container, which was subsequently filled to about 2/3 of its inner volume with water or 15%_wt ammonia solution. After closing the container with a Teflon lid, the reaction vessel was enclosed in a steel autoclave, heated to temperatures of 200 or 210 °C, kept at the chosen temperature under autogenous pressure for several days and then cooled to room temperature within three hours by removing the autoclave from the oven. The solid material obtained after the reaction time was filtered off through a glass frit, washed with mother liquor, water and ethanol and dried in air. Details of selected batches are given in Table 1. Crystals suitable for single-crystal X-ray diffraction studies were obtained from most of these experiments.

Table 1. Details for selected hydrothermal experiments to investigate foreign anion inclusions into M₃(TeO₃)₂(OH)₂ phases.

Batch	Educts	Molar Ratios	Reaction Medium	Duration/d; Temperature/°C
1 *	CoSO ₄ ·7H ₂ O, TeO ₂ , KOH	3:2:9	water	7; 210
2 *	Co(NO ₃) ₂ ·6H ₂ O, TeO ₂ , KOH	3:2:9	water	7; 210
3 *	MnCO ₃ , TeO ₂ , KOH	1:1:4	water	7; 210
4	MnCO ₃ , TeO ₂ , NaOH	1:1:4	water	7; 210
5 *	MnSO ₄ ·H ₂ O, TeO ₂ , KOH, K ₂ CO ₃	1:1:4:2	water	7; 210
6	MnSO ₄ ·H ₂ O, TeO ₂ , KOH	1:1:4	water	7; 210
7 *	MnSO ₄ ·H ₂ O, TeO ₂ , NaOH	1:1:4	water	7; 210
8 *	MnCl ₂ ·4H ₂ O, TeO ₂ , NaOH	1:1:4	water	7; 210
9 *	MnBr ₂ , TeO ₂ , NaOH	1:1:4	water	7; 210
10 *	MnSO ₄ ·H ₂ O, TeO ₂	3:1	ammonia	5; 210
11 *	NiSO ₄ ·6H ₂ O, TeO ₂	3:1	ammonia	5; 210
12 *	CoSeO ₄ ·5H ₂ O, TeO ₂	3:1	ammonia	5; 210
13 *	NiO, Fe(NO ₃) ₃ ·9H ₂ O, Mg(OH) ₂ , TeO ₂	1:1:1:1	water	68; 200

* Single-crystals of M₃(TeO₃)₂(OH)₂-type compounds isolated for X-ray diffraction studies.

2.2. Diffraction Measurements and Crystal-Structure Refinements

Powder X-ray diffraction (PXRD) measurements were performed on a PANalytical X'Pert II Pro type PW 3040/60 diffractometer (Malvern Panalytical Ltd., Malvern, UK) using Cu-K $_{\alpha 1,2}$ -radiation and an X'Celerator detector. For phase analysis and refinements of unit-cell parameters, the Highscore+ software suite was used [17].

Single-crystal X-ray diffraction studies were conducted on a Bruker Kappa Apex-II single crystal diffractometer (Bruker AXS Inc.: Madison, WI, USA) using graphite-monochromatized Mo-K $_{\alpha}$ -radiation equipped with a CCD area detector. Instrument software (APEX3, SAINT [18]) was used for optimized measurement strategies and data reduction. The intensity data were corrected for absorption effects with SADABS [19]. The crystal structures were solved with SHELXT [20], refined with SHELXL [21] and graphically represented with ATOMS [22].

The atom labels were assigned in accordance with the structure of isotypic Co $_3$ (TeO $_3$) $_2$ (OH) $_2$ [23]. Refinement of the framework structure including the metal position M1 and atoms Te1, Te2, O1–O $_4$ was straightforward. In some cases, the H1 atom attached to O $_4$ could be located from difference-Fourier maps and was included in the model with soft restraints on the O–H bond length (O–H = 0.9(1) Å). Smearred electron-density peaks originating from occupationally disordered sites located in large hexagonal channels characterize the remaining part of the crystal structures. Except for Co $_3$ (TeO $_3$) $_2$ (OH) $_2$ and Mn $_3$ (TeO $_3$) $_2$ (OH) $_2$ obtained from batch 2 and 3, respectively, which were modelled with full occupancy of O $_5$ (belonging to the OH group), in all other crystal-structure refinements, the presence of additional anions in the channels was considered for modelling. The site occupation factor (s.o.f.) of the heaviest element (S, Se, Cl, Br) was refined freely until convergence and then fixed. For SO $_4^{2-}$ and SeO $_4^{2-}$ groups, the corresponding s.o.f.s of participating O atoms were adapted to this value, and the s.o.f. of O $_5$ constrained to fulfil the criterion of electroneutrality. Although it is known that the (refined) occupancy correlates with the displacement parameters, we used this approach for simplicity. H atoms associated with the OH group in the channels could not be located and were not modelled but are considered in the formula and other crystallographic data. Crystal structure and refinement data are compiled in Table 2. Further details of the crystal structure investigations may be obtained from the joint CCDC/FIZ Karlsruhe online deposition service: <https://www.ccdc.cam.ac.uk/structures/> (accessed on 30 August 2022) by quoting the deposition numbers specified at the end of Table 2.

Numerical data of the related phases Co $_3$ (TeO $_3$) $_2$ (OH) $_2$ from batch 2 (apparent NO $_3^-$ inclusion not modelled), Co $_3$ (TeO $_3$) $_2$ (OH) $_{1.5}$ {(SO $_4$) $_{0.12}$ (OH) $_{0.26}$ } from batch 1, Mn $_3$ (TeO $_3$) $_2$ (OH) $_{1.5}$ {Cl $_{0.18}$ (OH) $_{0.32}$ } from batch 8, and Mn $_3$ (TeO $_3$) $_2$ (OH) $_{1.5}$ {(SO $_4$) $_{0.15}$ (OH) $_{0.20}$ } from batch 10 (with different modelling of the sulfate group in the channels) and their respective CSD deposition codes can be found in the Supplementary Material (Tables S1 and S2).

Table 2. Data collection and refinement details.

Empirical Formula	$\text{H}_2\text{Mn}_3\text{O}_8\text{Te}_2$	$\text{H}_{1.70}\text{Mn}_3\text{O}_{8.30}\text{S}_{0.15}\text{Te}_2$	$\text{Br}_{0.18}\text{H}_{1.82}\text{Mn}_3\text{O}_{7.82}\text{Te}_2$	$\text{H}_{1.60}\text{Mg}_3\text{O}_{8.40}\text{S}_{0.20}\text{Te}_2$	$\text{Co}_3\text{H}_{1.64}\text{O}_{8.36}\text{Se}_{0.58}\text{Te}_{1.60}$	$\text{H}_{1.60}\text{Ni}_3\text{O}_{8.40}\text{S}_{0.20}\text{Te}_2$
Structural Formula	$\text{Mn}_3(\text{TeO}_3)_2(\text{OH})_{1.5}\{\text{(OH)}_{0.5}\}$	$\text{Mn}_3(\text{TeO}_3)_2(\text{OH})_{1.5}\{\text{(SO}_4\text{)}_{0.15}(\text{OH})_{0.20}\}$	$\text{Mn}_3(\text{TeO}_3)_2(\text{OH})_{1.5}\{\text{Br}_{0.18}(\text{OH})_{0.32}\}$	$\text{Mg}_3(\text{TeO}_3)_2(\text{OH})_{1.5}\{\text{(SO}_4\text{)}_{0.2}(\text{OH})_{0.1}\}$	$\text{Co}_3(\text{TeO}_3)_{1.6}(\text{SeO}_3)_{0.4}(\text{OH})_{1.5}\{\text{(SeO}_4\text{)}_{0.18}(\text{OH})_{0.14}\}$	$\text{Ni}_3(\text{TeO}_3)_2(\text{OH})\{\text{(SO}_4\text{)}_{0.2}(\text{OH})_{0.1}\}^{1.5}$
Obtained from batch	5	7	9	13	12	11
M_r	550.04	559.34	561.15	470.68	562.10	573.89
Temp./°C	−173	23	23	23	25	−173
Cryst. dim./mm ³	0.09 × 0.04 × 0.03	0.11 × 0.02 × 0.02	0.12 × 0.02 × 0.02	0.30 × 0.01 × 0.01	0.09 × 0.01 × 0.01	0.05 × 0.01 × 0.01
Cryst. colour	light-yellow	light-yellow	light-yellow	colourless	blue	yellow
Cryst. form	prism	prism	prism	prism	lath	lath
Space group, No.	$P6_3mc$, 186	$P6_3mc$, 186	$P6_3mc$, 186	$P6_3mc$, 186	$P6_3mc$, 186	$P6_3mc$, 186
Formula units Z	4	4	4	4	4	4
$a/\text{Å}$	13.410(4)	13.4509(4)	13.4389(2)	13.0705(15)	13.0390(7)	12.9703(7)
$c/\text{Å}$	5.1393(17)	5.1410(2)	5.16780(10)	5.0381(6)	5.0199(4)	4.9441(3)
$V/\text{Å}^3$	800.3(6)	805.53(6)	808.28(3)	745.39(19)	739.12(10)	720.31(9)
μ/mm^{-1}	11.815	11.784	12.571	8.156	15.704	15.778
X-ray density/g·cm ^{−3}	4.565	4.612	4.611	4.194	5.051	5.292
$\theta_{\min}\text{--}\theta_{\max}/^\circ$	3.509–32.066	3.029–34.991	1.750–33.182	1.799–32.518	3.125–25.429	3.141–30.986
h range	−20–20	−20–21	−16–19	−19–19	−14–15	−17–18
k range	−20–20	−21–13	−20–20	−19–19	−15–15	−18–18
l range	−7–7	−8–8	−7–7	−7–7	−6–6	−7–7
Measured refl.	14,498	19,118	10,425	13,504	5006	6453
Independent refl.	1041	1300	1131	1006	516	858
Observed refl. ($I > 2\sigma(I)$)	992	1245	1059	856	455	794
R_{int}	0.0553	0.0443	0.0621	0.0978	0.0972	0.0809
$T_{\min}; T_{\max}$	0.5435; 0.7463	0.2816; 0.3604	0.5354; 0.7862	0.5652; 0.7464	0.4717; 0.7452	0.5554; 0.7462
No. of parameters	51	57	54	54	42	53
Flack parameter [24,25]	0.00(3) using 430 quotients	−0.01(2) using 547 quotients	−0.13(9) using 462 quotients	0.02(4) using 344 quotients	0.07(11)	0.01(5) using 330 quotients
$R1 (F^2 > 2\sigma(F^2))$	0.0201	0.0149	0.0317	0.0364	0.0337	0.0328
$wR2(F^2 \text{ all})$	0.0472	0.0351	0.0784	0.0855	0.0807	0.0707
GOF	1.118	1.044	1.072	1.066	1.055	1.059
CSD-deposition code	2,203,365	2,203,363	2,203,360	2,203,368	2,203,369	2,203,367

2.3. Energy-Dispersive X-ray Spectrometry (EDS)

Semiquantitative chemical analysis of carbon-coated, mechanically separated crystals was carried out using a JEOL JSM-6610LV (JEOL Ltd., Tokyo, Japan) scanning electron microscope (SEM) equipped with a high-sensitivity and high-resolution energy-dispersive X-ray spectrometer (Bruker e-FlashHR+; detector area 30 mm², resolution 127 eV) and Bruker Esprit 2.0 software (Bruker Nano GmbH, Berlin, Germany). Each spectrum was measured with an accelerating voltage of 15 kV for 60 s. No beam damage was noted. Several years of experience with this set-up show that the performed standardless analyses allow the derivation of chemical formulae that differ only 2–10% from the ideal formulae.

2.4. Raman Spectroscopy

Raman spectra were measured on randomly oriented crystals using a confocal micro-Raman spectrometer Renishaw RM1000 (Renishaw plc, Gloucestershire, UK) equipped with a 17 mW HeNe laser (632.8 nm) for excitation, an ultra-steep edge filter set facilitating measurements as close as >40 cm⁻¹ to the Rayleigh line, a Leica DLML microscope (Leitz, Wetzlar, Germany) with a 50×/0.75 objective, a 1200 lines/mm grating in a 300 mm monochromator and a thermo-electrically cooled CCD detector. The entrance slit and CCD readout were set to quasi-confocal mode. The resolution of the system (apparatus function) was 3–4 cm⁻¹, and the Raman shift of the instrument was calibrated by the Rayleigh line and the 520.5 cm⁻¹ line of a Si standard. Spectra were acquired over 120 s to obtain a good signal-to-noise ratio. Full laser power (100%) could be used for crystals from batches 4, 8 and 9, whereas the Co-compounds from batches 1 and 2 required attenuation of the laser to 25% and 10%. The spectral range was extended from 4000 to –20 cm⁻¹ in order to include the Rayleigh line as an internal standard. Instrument set-up and control were controlled with Grams32 software. Baseline handling and peak-fitting with Lorentz-peaks were done using the program fityk [26] using the Levenberg-Marquardt algorithm.

3. Results and Discussion

3.1. Synthesis

$M_3(\text{TeO}_3)_2(\text{OH})_2$ compounds with $M = \text{Ni}, \text{Co}$ are known and have been prepared hydrothermally from MO and TeO_2 in diluted HCl solution at 380 °C and 900 bar [23]. Under these conditions, an inclusion of Cl^- likewise appears to be possible, but chemical analysis showed no amount of Cl in the crystals [23]. During the current study, we have worked under considerably lower temperatures and autogenous pressures for the hydrothermal set-up, but under alkaline conditions, because otherwise the solubility of TeO_2 is not sufficient at the given temperature-pressure conditions.

Just as it was the case for the intended preparation of single-phase material in the $\text{Mn}^{\text{II}}/\text{Te}^{\text{IV}}/\text{O}/(\text{H})$ system [14], phase purity could not be achieved during the current study for preparation of $M_3(\text{TeO}_3)_2(\text{OH})_2$ ($M = \text{Mg}, \text{Mn}, \text{Co}, \text{Ni}$) compounds. In all batches, phase mixtures were obtained, as revealed by phase analysis on basis of PXRD data (see Supplementary Material, Figure S1). All batches compiled in Table 1 at least yielded $M_3(\text{TeO}_3)_2(\text{OH})_2$ -type phases as byproducts, frequently in form of prismatic hexagonal crystals (Figure 1). The refined composition of crystals from the different batches is provided in Table 2. Due to the distinct hexagonal prismatic form of the $M_3(\text{TeO}_3)_2(\text{OH})_2$ -type crystals, the PXRD pattern of the bulk show strong texture effects (Figure S1).

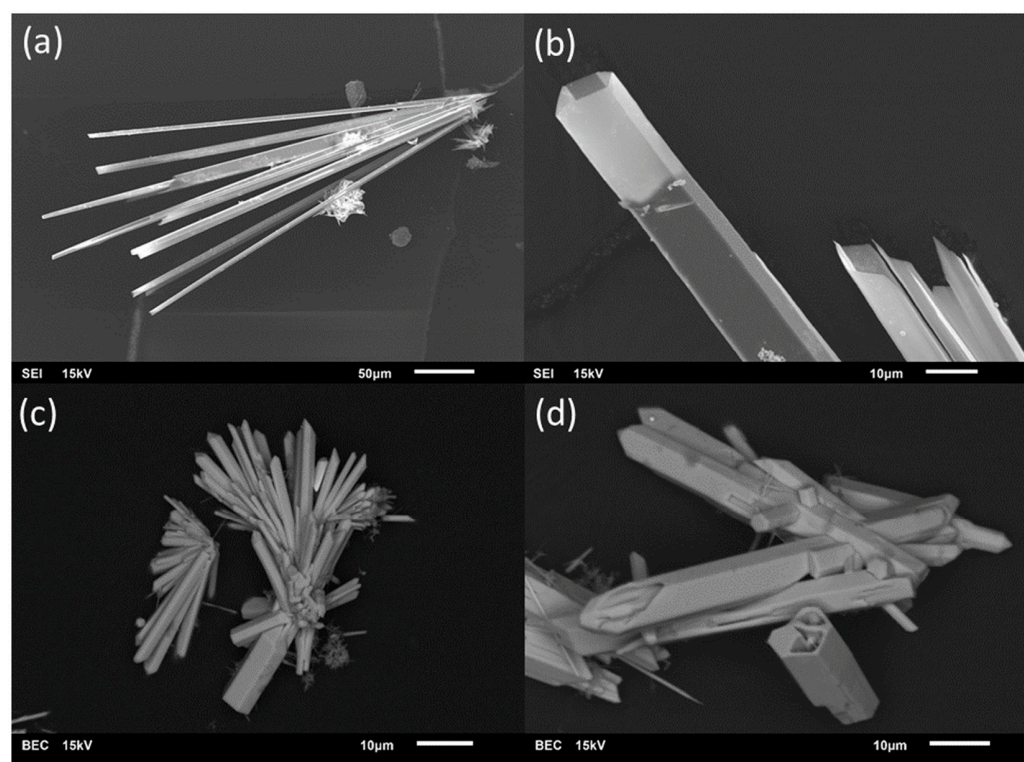


Figure 1. Representative for the entire $M^{II}_3(\text{TeO}_3)_2(\text{OH})_2$ -type series ($M = \text{Mg}, \text{Mn}, \text{Co}, \text{Ni}$), SEM photographs of $\text{Mg}_3(\text{TeO}_3)_2(\text{OH})_{1.5}\{(\text{SO}_4)_{0.2}(\text{OH})_{0.10}\}$ (a,b) and of $\text{Mn}_3(\text{TeO}_3)_2(\text{OH})_{1.5}\{\text{Cl}_{0.18}(\text{OH})_{0.32}\}$ (c,d) show the characteristic hexagonal prismatic form of the crystals. The crystals frequently aggregate in sprays and have hollow terminations, suggesting growth under conditions of local oversaturation. The images are either secondary electron images (SEI) or backscattered electron contrast (BEC) images.

Next to other known phases in variable yields, e.g., $\text{M}_2\text{Te}_3\text{O}_8$ [11] and $\text{MTe}_6\text{O}_{13}$ [9,27] as main phases, the non-reacted educt TeO_2 and M_3O_4 phases ($M = \text{Co}, \text{Mn}$) together with elemental Te were sometimes found in the product mixtures. In several batches, also some reflections in the PXRD pattern could not be assigned during phase analysis, indicating the presence of yet unknown phases. Similar problems for preparation of single-phase material were reported for $\text{Co}_3(\text{TeO}_3)_2(\text{OH})_2 \cdot \sim 0.45 \text{H}_2\text{O}$ under similar hydrothermal conditions [28]. The high number of adjustable and interdependent parameters such as molar educt ratio, concentration, temperature, duration, pH value, etc., causes this behaviour. Thus, these parameters need to be varied and optimized for each batch, which, in most cases, is a laborious undertaking [28].

The presence of phase mixtures precluded bulk measurements such as thermogravimetry as a complementary analytical method for confirmation of the chemical composition, here in particular with respect to the amount of OH^- and/or water, and NO_3^- or CO_3^{2-} in the crystals. Thus, analyses of the chemical composition with respect to additionally incorporated groups, as refined in the respective crystal structure models, were performed with selected single crystals of the $M^{II}_3(\text{TeO}_3)_2(\text{OH})_2$ series and are based upon SEM-EDS measurements and Raman spectroscopy.

3.2. Crystal Structures

The phases with idealized composition $M^{\text{II}}_3(\text{TeO}_3)_2(\text{OH})_2$ ($M = \text{Mg}, \text{Mn}, \text{Co}, \text{Ni}$) crystallize isotypically in the non-centrosymmetric hexagonal space group type $P6_3mc$. Hydrothermally synthesized $\text{Co}_3(\text{TeO}_3)_2(\text{OH})_2$ and $\text{Ni}_3(\text{TeO}_3)_2(\text{OH})_2$ have been reported as the first representatives of the $M_3(\text{TeO}_3)_2(\text{OH})_2$ family, with the crystal structure determined on basis of single-crystal X-ray data. Since the $M_3(\text{TeO}_3)_2(\text{OH})_2$ structure type has already been described in detail [23], here only the most important aspects of the crystal structure are given.

The asymmetric unit of the $M_3(\text{TeO}_3)_2(\text{OH})_2$ structure type comprises ten atoms. Atom O_5 , which is part of an OH group, is located on a site with site symmetry $3m$. (multiplicity 2, Wyckoff letter a), Te_2 likewise is situated on a site with symmetry $3m$. ($2b$), Te_1 , O_1 , O_3 , O_4 (that is also part of an OH group) and H_1 on sites with symmetry $.m$. ($6c$), and M_1 and O_2 are located on the general position ($12d$). So far, the position of the H atom bonded to O_5 remains undetermined.

In the $M_3(\text{TeO}_3)_2(\text{OH})_2$ structure type, the two isolated trigonal-pyramidal $[\text{TeO}_3]$ units, each described with Q^{3000} in the notation of Christy et al. [29], and $[\text{MO}_4(\text{OH})_2]$ octahedra share common corners and edges, thus forming a framework structure with the composition $M^{\text{II}}_3(\text{TeO}_3)_2(\text{OH})_{1.5}^{0.5+}$. The Te–O bond lengths range between 1.8 and 1.9 Å, which is characteristic for isolated $[\text{TeO}_3]$ groups [29]; secondary Te–O bonds typically associated with more distant O atoms situated between 2.7–3.5 Å [29] are found for Te_1 (≈ 3.0 Å), but not for Te_2 . The M–O bond lengths likewise are in the usual ranges (Table 3) for six-coordinate metal cations M^{II} (Mg: 2.089 Å [30]; Mn: 2.199 Å; Co: 2.108 Å; Ni: 2.070 Å [31]) and differ mainly due to the size of the M^{II} cation (ionic radii [32] for coordination number 6: 0.72 Å for Mg, 0.83 Å for Mn (high-spin configuration), 0.745 Å for Co (high-spin configuration) and 0.69 Å for Ni). Within the framework structure, only weak hydrogen-bonding interactions [33] between the OH donor group and the O_3 acceptor atom exist, with $\text{O}_4 \cdot \text{O}_3$ distances in the range between 3.10 [28] and 3.13 Å (Table 3). The $5s^2$ lone-pair electrons (E) situated at the Te^{IV} atoms are stereochemically active [34] and point to the free space of the structure, i.e., parallel to trigonal channels for Te_2 and to the centre of large hexagonal channels for Te_1 . Both types of channels extend parallel to $[001]$. The remaining OH^- counter anions associated with O_5 are accommodated in the centre of the large hexagonal channels. The diameter of these channels amounts to ≈ 6.5 Å when the space requirement of the lone-pair electrons E situated at Te_1 is neglected, and to ≈ 4.6 Å when considered. Thus, O_5 has no framework oxygen atoms within typical interaction distances for classical hydrogen bonding (shortest $\text{O} \cdot \text{O}$ distance ≈ 4.1 Å to O_2). Therefore, it appears likely that O_5 shows weak bonding interactions to the surrounding lone-pair electrons E of the $[\text{Te}_1\text{O}_3]$ units, as has been discussed for apparent stabilizing $E \cdot X$ interactions in the cubic $M_3\text{Te}_2\text{O}_6X_2$ ($M = \text{Sr}, \text{Ba}; X = \text{Cl}, \text{Br}$) structure family where the X^- anions are likewise located in large channels without notable interactions to the surrounding framework [35].

Table 3. Selected interatomic distances/Å in the crystal structures of $M_3(\text{TeO}_3)_2(\text{OH})_{1.5}^{0.5+}\{(X_x/n)(\text{OH})_{0.5-x}\}^{0.5-}$ ($0.5 \leq x \leq 0$) compounds.

	$\text{Mn}_3(\text{TeO}_3)_2(\text{OH})_{1.5}(\text{OH})_{0.5}$	$\text{Mn}_3(\text{TeO}_3)_2(\text{OH})_{1.5-}\{\text{SO}_4\}_{0.15}(\text{OH})_{0.20}\}$	$\text{Mn}_3(\text{TeO}_3)_2(\text{OH})_{1.5-}\{\text{Br}_{0.18}(\text{OH})_{0.32}\}$
M1—O ₂	2.113(4)	2.122(3)	2.137(7)
M1—O ₁	2.119(3)	2.137(2)	2.142(5)
M1—O ₃	2.169(4)	2.171(3)	2.175(7)
M1—O ₂	2.201(4)	2.217(2)	2.227(6)
M1—O ₄	2.219(4)	2.218(3)	2.231(6)
M1—O ₄	2.347(4)	2.339(3)	2.333(6)
Te1—O ₂ (2 ×)	1.877(4)	1.874(2)	1.871(6)
Te1—O ₁	1.910(5)	1.883(4)	1.898(9)
Te2—O ₃ (3 ×)	1.854(6)	1.852(4)	1.851(9)
O ₄ —H1	0.87(3)	0.97(3)	1.0(3)
H1—O ₄ · O ₃	3.111(10)	3.124(9)	3.122(11)
	$\text{Mg}_3(\text{TeO}_3)_2(\text{OH})_{1.5-}\{\text{SO}_4\}_{0.2}(\text{OH})_{0.1}\}$	$\text{Co}_3(\text{TeO}_3)_{1.6}(\text{SeO}_3)_{0.4-}(\text{OH})_{1.5}\{\text{SeO}_4\}_{0.18}(\text{OH})_{0.14}\}$	$\text{Ni}_3(\text{TeO}_3)_2(\text{OH})_{1.5-}\{\text{SO}_4\}_{0.2}(\text{OH})_{0.1}\}$
M1—O ₂	2.031(8)	2.035(11)	2.014(8)
M1—O ₁	2.060(6)	2.097(9)	2.065(5)
M1—O ₃	2.049(9)	2.097(11)	2.040(8)
M1—O ₂	2.090(7)	2.085(10)	2.032(7)
M1—O ₄	2.130(9)	2.157(12)	2.124(7)
M1—O ₄	2.240(9)	2.220(12)	2.172(8)
Te1—O ₂ (2 ×)	1.880(6)	1.851(10)	1.885(7)
Te1—O ₁	1.866(10)	1.862(17)	1.912(11)
Te2—O ₃ (3 ×)	1.832(11)	1.750(15)	1.886(10)
O ₄ —H1	—	—	—
H1—O ₄ · O ₃	—	—	—

However, the distance between symmetry-related O₅ atoms within the channels is ≈ 2.57 Å, which points to rather strong possible hydrogen-bonding interactions [33] along the channel direction. The principal set-up of the $M_3(\text{TeO}_3)_2(\text{OH})_2$ structure type is given in Figure 2. As depicted in Figure 2a, the O₅ atom exhibits a very large U_{eq} parameter. If O₅ is refined with anisotropic displacement parameters (ADP), a pronounced displacement in form of elongated ellipsoids along the channel direction is observed (Figure 2b). The reason for this behavior is obvious, since O₅ is not directly linked to the framework but shows strong interactions only to its symmetry-related counterparts along the channel direction. Aside from that, the large displacement parameter of O₅ indicates a possible disorder around the position with $3m$. site symmetry. This feature was observed for all $M_3(\text{TeO}_3)_2(\text{OH})_2$ -type crystals, irrespective of the batch or the two measurement temperatures (RT and -173 °C). Hence, this disorder appears to be characteristic for the $M_3(\text{TeO}_3)_2(\text{OH})_2$ structure type. All attempts to model this kind of disorder by introducing split positions led to unsatisfactory results, and O₅ was eventually modelled with only one site and a large displacement parameter.

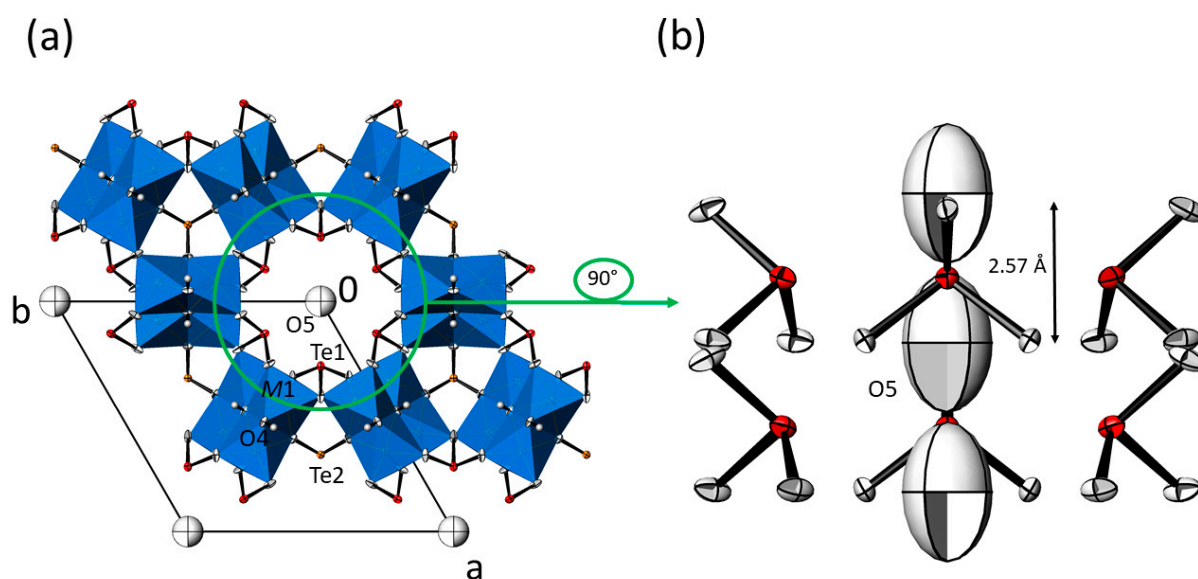


Figure 2. (a) Crystal structure of the isotypic $M_3(\text{TeO}_3)_2(\text{OH})_2$ family of compounds (data from $\text{Mn}_3(\text{TeO}_3)_2(\text{OH})_2$) in a projection along the hexagonal axis. $[\text{M1O}_6]$ octahedra (blue) are given in the polyhedral representation, and displacement ellipsoids are drawn at the 90% probability level; except O_5 refined with isotropic displacement parameters, all other non-H atoms were refined with anisotropic displacement parameters. (b) The content of the hexagonal channel with surrounding $[\text{Te1O}_3]$ units and the O_5 atom in the centre; all atoms are displayed with anisotropic displacement parameters at the 90% probability level. The indicated distance refers to adjacent O_5 sites.

Dependent on the employed metal salt as the M^{II} source, additional high remaining positive electron densities were noticed within the channels in the vicinity of O_5 . Using SO_4^{2-} , SeO_4^{2-} or X^- ($\text{X} = \text{Cl}, \text{Br}$) as anion groups of the metal salt, the remaining but smeared electron densities were much higher than in the case of CO_3^{2-} or NO_3^- as counter anions. In fact, for the crystals grown from metal sulfate, selenate or metal halide solutions, SO_4^{2-} and SeO_4^{2-} groups (using restraints on the S–O or Se–O distances) and X^- ($\text{X} = \text{Cl}, \text{Br}$) anions, respectively, could be modelled. Difference maps, representative of the entire $M^{\text{II}}_3(\text{TeO}_3)_2(\text{OH})_2$ -type series, are shown for $\text{Mn}_3(\text{TeO}_3)_2(\text{OH})_{1.5}\{\text{SO}_4\}_{0.15}(\text{OH})_{0.20}$ in Figure 3.

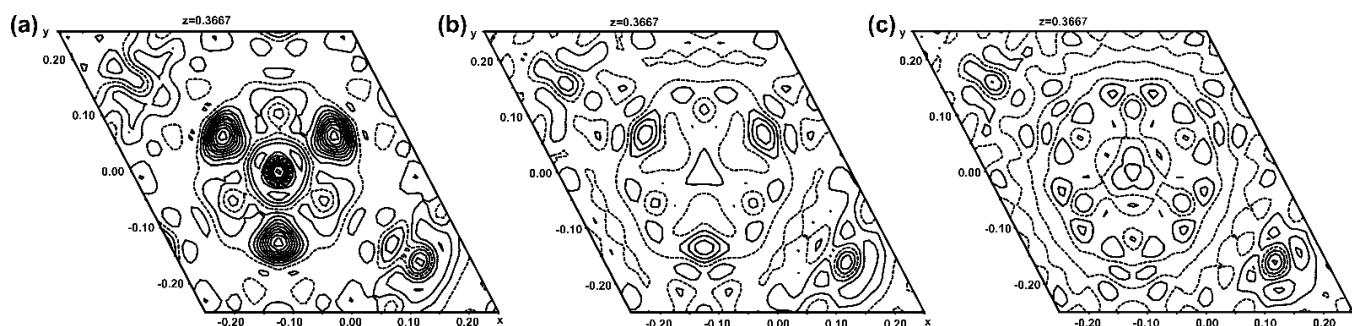


Figure 3. Difference contour maps showing an intersection perpendicular to the channel direction at the centre of the channel and with a height of $z = 0.3667$. Contour lines are shown at intervals of $0.2 \text{ e}^- \text{ \AA}^{-3}$ with cut-offs for minimum and maximum values of -1.5 and $3.0 \text{ e}^- \text{ \AA}^{-3}$, respectively. In (a), only O_5 is modelled in the channel, and positive electron density (continuous lines) at the centre (S atom) and from three surrounding O atoms is clearly visible. The remaining electron density nearly vanishes by modelling the sulfate group with one S and two O sites in (b) (see Figure 4), or with one S and three O sites in (c) (see Supplementary Material, Figure S2).

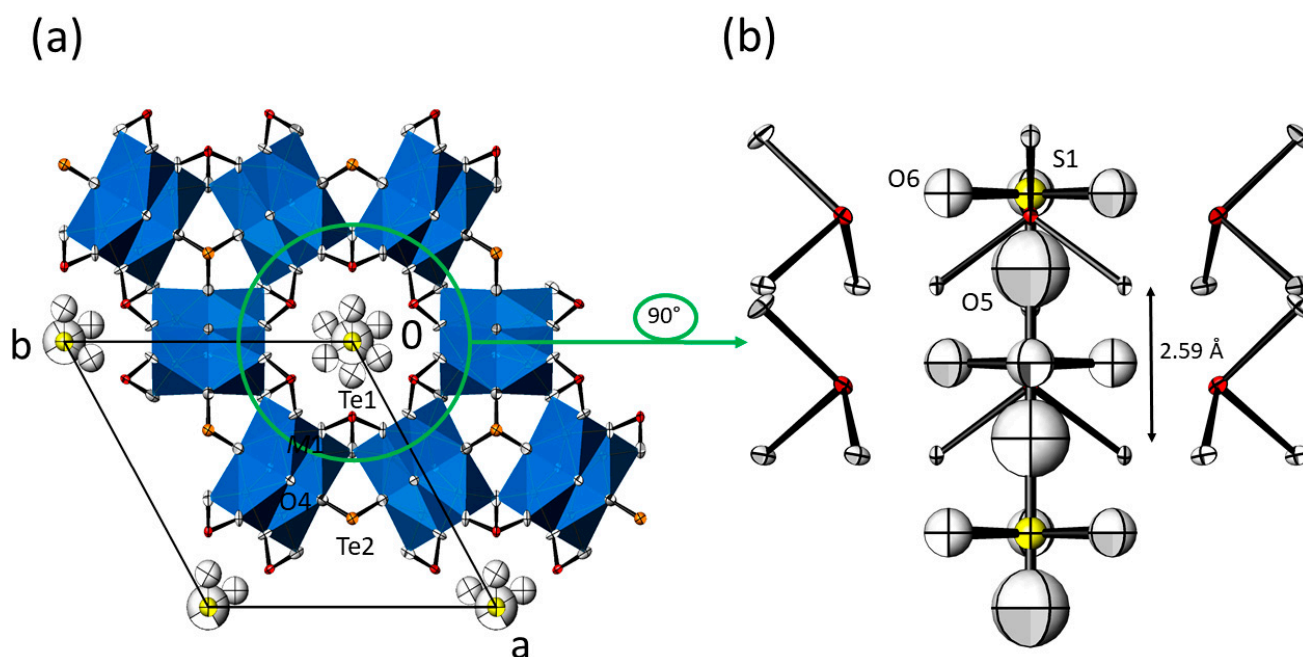


Figure 4. (a) Crystal structure of the $M_3(\text{TeO}_3)_2(\text{OH})_2$ family of compounds with additional SO_4^{2-} ions in the hexagonal channels (data from $\text{Mn}_3(\text{TeO}_3)_2(\text{OH})_{1.5}(\text{SO}_4)_{0.15}(\text{OH})_{0.20}$). Displacement ellipsoids are drawn at the 90% probability level (isotropic for O₅ and the sulfate group; anisotropic for all other atoms). (b) The content of the hexagonal channel with surrounding [Te₁O₃] units, and the O₅ atom and the sulfate group in the centre. The indicated distance refers to adjacent O₅ sites.

Like the O₅ atom of the OH[−] group, the additional anions present in the channels are situated on the 6₃ screw axis. Interdependent from each other, the corresponding anions present in the channels are occupationally disordered with the OH[−] group and are characterized by likewise large displacement parameters (Figures 4 and 5). Again, this feature is indicative of further disorder of the incorporated groups, and most probably interrelated with the (non-modelled) positional disorder of O₅. This is a typical case, where single crystal diffraction reveals its inherent limitations, leading to an averaged (and idealized) picture over the entire crystal. Nevertheless, modelling of incorporated XO_4^{2-} groups for $M = \text{Mg}, \text{Co}$ and Ni with X situated on the 6₃ screw axis (2 *a*; site symmetry 3*m*.), O₅ as one vertex and O₆ situated on a mirror plane (6 *c*; *m*.) together with its two symmetry-related O₆' and O₆'' vertex atoms led to a satisfying tetrahedral shape. In the case of $M = \text{Mn}$, the X site is situated at the same height (in *z*) as the three O₆ atoms, resulting in an unrealistic trigonal-planar arrangement with an additional capping O₅ atom (Figure 4b). Splitting O₅ into two further positions (O₇, O₈) on the mirror plane resulted in a more realistic tetrahedral arrangement but with a tilted orientation of the disordered XO_4^{2-} group relative to the 6₃ axis (see Supplementary Material, Figure S2).

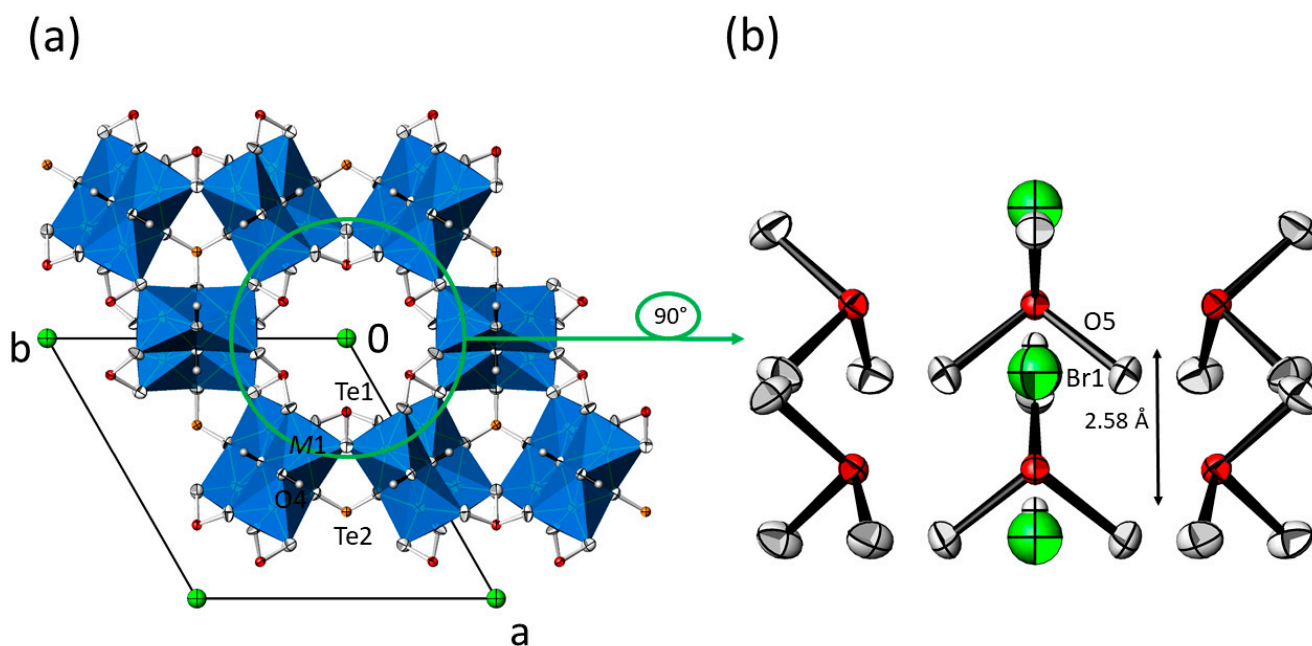


Figure 5. (a) Crystal structure of the $M_3(\text{TeO}_3)_2(\text{OH})_2$ family of compounds with additional X^- ions in the hexagonal channels (data from $\text{Mn}_3(\text{TeO}_3)_2(\text{OH})_{1.5}\{\text{Br}_{0.18}(\text{OH})_{0.32}\}$). Displacement ellipsoids are drawn at the 90% probability level (isotropic for O₅ and Br1; anisotropic for all other atoms). (b) The content of the hexagonal channel with surrounding $[\text{Te}_1\text{O}_3]$ units, and the O₅ site and the Br1 site in the centre. The indicated distance refers to adjacent O₅ sites.

For the lighter CO_3^{2-} or NO_3^- anion groups, modelling of their presence in the hexagonal channels did not lead to satisfactory results, although the existence of these groups is indicated by peaks of small remaining positive electronic densities more than 1 Å away from the hexagonal axis, and evidenced by spectroscopic measurements, as discussed below. A special case pertains to the use of CoSeO_4 as the Co^{II} source for growth of $\text{Co}_3(\text{TeO}_3)_{1.6}(\text{SeO}_3)_{0.4}(\text{OH})_{1.5}\{(\text{SeO}_4)_{0.18}(\text{OH})_{0.14}\}$ crystals. Similar to the sulfates, small amounts of occupationally disordered SeO_4^{2-} groups then are incorporated within the hexagonal channels. In addition, SeO_3^{2-} anion groups exclusively substitute most parts of the $[\text{Te}_2\text{O}_3]$ units in the framework structure (occupation ratio $\text{Se}_2:\text{Te}_2 = 0.80(3):0.20(3)$), as can be seen by the considerably shortened (Se,Te)₂-O distances of 1.750(15) Å in comparison with the typical Te-O distance (Table 3). The $[\text{Te}_1\text{O}_3]$ unit, however, is not substituted in the present case, and the corresponding Te1-O distances are normal, indicative of a clear preference of Se for the Te2 site. Hydrothermal synthesis and crystal structure refinement (based on PXRD data) were reported for the pure end-member $\text{Co}_3(\text{SeO}_3)_2(\text{OH})_2$ [36]. This phase likewise adopts the $M_3(\text{TeO}_3)_2(\text{OH})_2$ structure type where the SeO_3^{2-} groups replace the TeO_3^{2-} groups. The presence of such SeO_3^{2-} groups in $\text{Co}_3(\text{TeO}_3)_{1.6}(\text{SeO}_3)_{0.4}(\text{OH})_{1.5}\{(\text{SeO}_4)_{0.18}(\text{OH})_{0.14}\}$, however, requires a partial reduction of the employed $\text{Se}^{\text{VI}}\text{O}_4^{2-}$ to $\text{Se}^{\text{IV}}\text{O}_3^{2-}$. Such a situation is not uncommon for hydrothermal syntheses where different (unwanted) redox reactions can occur between the constituents, frequently leading to phase mixtures. As noted in Section 3.1., mixed-valent $M_3\text{O}_4$ phases were identified in some of the batches. The M^{II} cations, partially oxidized to M^{III} cations, may react as a reductant for Se^{VI} .

The influence of the type of incorporated anion or (hypothetically) also of water on the unit-cell parameters was examined on the basis of single-crystal and powder X-ray diffraction measurements, neglecting different measurement temperatures. Experience shows that the volume of the unit-cell is about 1–2% smaller at -173°C than at room-temperature, provided that no phase-transformations occur. Corresponding unit-cell parameters for Co- and Mn-containing phases and of $\text{Co}_3(\text{TeO}_3)_2(\text{OH})_2$ and $\text{Co}_3(\text{TeO}_3)_2(\text{OH})_2 \cdot \sim 0.45\text{H}_2\text{O}$

as references are collated in Table 4. The unit-cell parameters of $\text{Co}_3(\text{TeO}_3)_2(\text{OH})_2$ are considerably smaller than those of its slightly hydrated form. The unit-cell parameters of the $\text{Co}_3(\text{TeO}_3)_2(\text{OH})_2$ phases with additional incorporated anions (SO_4^{2-} , NO_3^-) lie between those of the two forms. In order to rule out possibly incorporated crystal water molecules inside the channels, the powder samples from batch 1 and 2 were heat-treated at 210 °C for three days and measured again directly afterwards (see Supplementary Material, Figure S1). The temperature of 210 °C should be sufficient for the release of potential crystal water, as for $\text{Co}_3(\text{TeO}_3)_2(\text{OH})_2 \cdot \sim 0.45\text{H}_2\text{O}$ the evaporation of water molecules is reported to start at 100 °C and to be finished around 195 °C based on Raman, TGA and MS analyses [28]. For the present samples, a significant change of the unit-cell parameters before and after heat-treatment was not observed, demonstrating that crystal water was not present in the samples and that the incorporated anions cause the increase of the unit-cell volume relative to $\text{Co}_3(\text{TeO}_3)_2(\text{OH})_2$.

Table 4. Unit-cell parameters of samples to investigate foreign anion inclusion into $M_3(\text{TeO}_3)_2(\text{OH})_2$ phases. Batch numbers refer to Table 1.

Batch	M	Possible Inclusions	Measurement	T/°C	a/Å	c/Å	V/Å ³
1	Co	SO_4^{2-} , OH^-	powder	25	13.1146(7)	5.0475(3)	751.8
			single-crystal	−173	13.1102(7)	5.0179(4)	746.9
1 *			powder	25	13.1186(7)	5.0335(3)	750.2
2	Co	NO_3^- , OH^-	powder	25	13.1126(7)	5.0452(3)	751.3
			single-crystal	−173	13.0907(4)	5.02810(10)	746.2
2 *			powder	25	13.1127(8)	5.0394(3)	750.4
3	Mn	CO_3^{2-} , OH^-	powder	25	13.42771(15)	5.16593(7)	806.7
			single-crystal	−173	13.3999(4)	5.1359(2)	798.6
4	Mn	CO_3^{2-} , OH^-	powder	25	13.4171(3)	5.16516(11)	805.3
5	Mn	SO_4^{2-} , CO_3^{2-} , OH^-	powder	25	13.4271(3)	5.16877(10)	807.0
			single-crystal	−173	13.4082(5)	5.1371(3)	799.8
			single-crystal	−173	13.410(4)	5.1393(17)	800.5
6	Mn	SO_4^{2-} , OH^-	powder	25	13.4779(2)	5.16844(10)	813.1
7	Mn	SO_4^{2-} , OH^-	powder	25	13.4902(5)	5.1673(2)	814.4
			single-crystal	−173	13.4216(7)	5.1712(4)	806.7
8	Mn	Cl^- , OH^-	powder	25	13.4206(2)	5.17517(8)	807.2
			single-crystal	25	13.4364(4)	5.1738(3)	808.9
9	Mn	Br^- , OH^-	powder	25	13.4383(2)	5.17202(8)	808.9
			single-crystal	25	13.4389(2)	5.16780(10)	808.3
		OH^-	single-crystal	25	13.034(6)	5.016(3)	738.0
		OH^- , H_2O	single-crystal	25	13.164(1)	5.0321(6)	755.2

* after heat treatment at 210 °C for three days.

For the Mn-compounds obtained from batches 3–9, a clear dependence of unit-cell parameters from incorporated anions is difficult to deduce because a reference material without additional anions, like for $\text{Co}_3(\text{TeO}_3)_2(\text{OH})_2$, has not been reported so far. From the given data, it can be seen that the unit-cell volumes of samples with CO_3^{2-} , Cl^- or Br^- as possible additional anions are very similar. Only for samples from batches 6 and 7 containing the considerably bigger SO_4^{2-} anion groups, a significant increase of the unit-cell volume is noticed. On the other hand, the data for batch 5 with SO_4^{2-} and CO_3^{2-} simultaneously present in the reaction mixture suggest that only a minor amount of sulfate, if any, is incorporated in the crystals, indicating a preferred incorporation of CO_3^{2-} over SO_4^{2-} anion groups.

However, the diameter of the hexagonal channel in the $M_3(\text{TeO}_3)_2(\text{OH})_2$ structure type, as calculated from opposite Te··Te distances at the same height, correlates with the size of the incorporated foreign group (radius $\text{OH}^- = 1.33 \text{ \AA}$, $\text{Cl}^- = 1.72 \text{ \AA}$, $\text{Br}^- = 1.88 \text{ \AA}$, $\text{SO}_4^{2-} = 2.58 \text{ \AA}$, $\text{SeO}_4^{2-} = 2.49 \text{ \AA}$ [37]; $\text{H}_2\text{O} = 1.35 \text{ \AA}$ [38]). Due to this effect, the channel diameter increases from 6.412 Å in $\text{Co}_3(\text{TeO}_3)_2(\text{OH})_2$ [23] upon incorporation of water to 6.604 Å in $\text{Co}_3(\text{TeO}_3)_2(\text{OH})_2 \cdot \sim 0.45\text{H}_2\text{O}$ [28], to 6.535 Å in $\text{Co}_3(\text{TeO}_3)_2(\text{OH})_{1.5}(\text{SO}_4)_{0.12}(\text{OH})_{0.26}$, or to 6.526 Å with additional oxidoselenate(VI) anions in the channels in $\text{Co}_3(\text{TeO}_3)_{1.6}(\text{SeO}_3)_{0.4}$

(OH)_{1.5}{(SeO₄)_{0.18}(OH)_{0.14}} (this work). In comparison with the incorporation of water, the bigger size of the oxidoselenate(VI) anion suggests also a larger size of the channel diameter. However, in Co₃(TeO₃)_{1.6}(SeO₃)_{0.4}(OH)_{1.5}{(SeO₄)_{0.18}(OH)_{0.14}} parts of the [TeO₃] groups in the framework structure are substituted by smaller SeO₃²⁻ anions, which makes the framework itself smaller and thus is not suitable for direct comparison. The above mentioned trend can also be seen when additional sulfate anions are hosted in the channels, with a resulting increase of the channel diameter from 6.459 Å in Ni₃(TeO₃)₂(OH)₂ [23] to 6.477 Å in Ni₃(TeO₃)₂(OH)_{1.5}{(SO₄)_{0.2}(OH)_{0.1}} (this work), and is obvious for the series Mn₃(TeO₃)₂(OH)₂ (6.538 Å), Mn₃(TeO₃)₂(OH)_{1.5}{Cl_{0.18}(OH)_{0.32}} (6.553 Å), Mn₃(TeO₃)₂(OH)_{1.5}{Br_{0.18}(OH)_{0.32}} (6.578 Å), and Mn₃(TeO₃)₂(OH)_{1.5}{(SO₄)_{0.15}(OH)_{0.20}} (6.617 Å).

3.3. EDS

Since no internal calibration was conducted for the individual SEM-EDS measurements, the absolute values of the determined atomic contents are of less significance, but at least semi-quantitative deductions can be made from each measurement. The light elements N and C were below EDS detection limits in all cases; H atoms were not considered for the determined composition (in %_{at}).

For the hexagonal prismatic crystals of the Co-compounds obtained from batches 1 and 2 (employed salts: CoSO₄·7H₂O and Co(NO₃)₂·6H₂O), various point analyses on two different crystals revealed an average Co:Te atomic ratio (ideal 1.5) of 1.56 for batch 1 and 1.54 for batch 2, respectively. The averaged sulfur content was determined to 1%_{at} for crystals of batch 1 (expected value for the refined composition Co₃(TeO₃)₂(OH)_{1.5}{(SO₄)_{0.12}(OH)_{0.26}} = 0.9%_{at}).

Crystals from batches 8 and 9 (employed salts: MnCl₂ and MnBr₂) consisted of rather large hexagonal prisms (Figure 1c,d). For both samples, an Mn:Te ratio slightly below the expected value of 1.5 was determined, viz. 1.38 for crystals from batch 8 (averaged from four measurement points) and 1.37 for sample 9 (averaged from five measurement points). The determined averaged halogen content of 2.8%_{at} Cl and 3.1%_{at} Br is significantly higher than that in the refined composition from single-crystal diffraction data (Mn₃(TeO₃)₂(OH)_{1.5}{X_{0.18}(OH)_{0.32}}; X = Cl, Br; ideal 1.4%_{at}). Crystals from batch 7 (employed salt: MnSO₄) had the form of small hexagonal needles. An Mn:Te ratio of 1.43 on average from three measurement points and a sulfur content of 1.5%_{at} (ideal 1.1%_{at} for the refined composition Mn₃(TeO₃)₂(OH)_{1.5}{(SO₄)_{0.15}(OH)_{0.20}}) were determined. SEM-EDS analyses of the crystals from batches 3 and 5 (employed salts: MnCO₃ and MnSO₄ in a K₂CO₃ solution) revealed no presence of heavy elements other than Mn and Te in ratios of 1.48 and 1.54 (from two and three measurement points on different crystals). Therefore, it can be deduced that CO₃²⁻ ions are preferably incorporated compared to SO₄²⁻ ions, if both are present in the solution (as in batch 5).

The colourless crystals from batch 13 (Figure 1a,b), obtained from a multi-metal mixture (employed salts: NiO, Fe(NO₃)₃·9H₂O, Mg(OH)₂), showed only the presence of Mg as the metal. Again, the Mg:Te ratio of 1.38 averaged from five measurement points is in fair agreement with the ideal value of 1.5. Although the employed salts were free from sulfur, this element was clearly detected in the EDS measurement, albeit with a much lower amount of 0.4%_{at} than expected (1.5%_{at} for an assumed composition of Mg₃(TeO₃)₂(OH)_{1.5}{(SO₄)_{0.2}(OH)_{0.1}}). We suspect that the sulfur source originates from a polluted Teflon container that had been used in the series of batches (including sulfates) conducted during the present study. It should also be noted that in some of the EDS analyses Na and Si were detected in very small amounts of ≈1%_{at}. We can only speculate about the origin of these elements. Insufficient washing of crystals grown in NaOH-containing solutions and abrasion from glass containers are probable sources.

3.4. Raman Spectroscopy

Raman spectra of investigated samples from batches 1, 2, 4, 8 and 9 exhibit similar general features, with bands subdivided into three main groups. The O–H-stretching vibrations occur in the region 3600–3400 cm^{-1} , bands originating from incorporated anions in the region 1100–900 cm^{-1} , and bands from Te–O, M–O and lattice vibrations in the region below 800 cm^{-1} .

Raman-spectra of the Co-compounds obtained from batches 1 (SO_4^{2-} as counter anion) and 2 (NO_3^- as counter anion) in general show very similar band positions with one major exception in the range between 1100 and 900 cm^{-1} (Figure 6). The corresponding band in the crystal from batch 1 is at 971 cm^{-1} and does not appear in any of the other investigated samples from batches 2, 4, 8 and 9. This band corresponds to the symmetrical stretching vibration of the SO_4^{2-} group and is comparable to the band at 981 cm^{-1} for Na_2SO_4 [39]. Crystals from batch 2, instead, exhibit a rather sharp Raman band at 1044 cm^{-1} , corresponding to the symmetrical stretching mode of the NO_3^- group, which is at 1050 cm^{-1} for alkali metal nitrates [39]. Thus, this is a strong confirmation that SO_4^{2-} and NO_3^- units, respectively, are incorporated in the hexagonal channels.

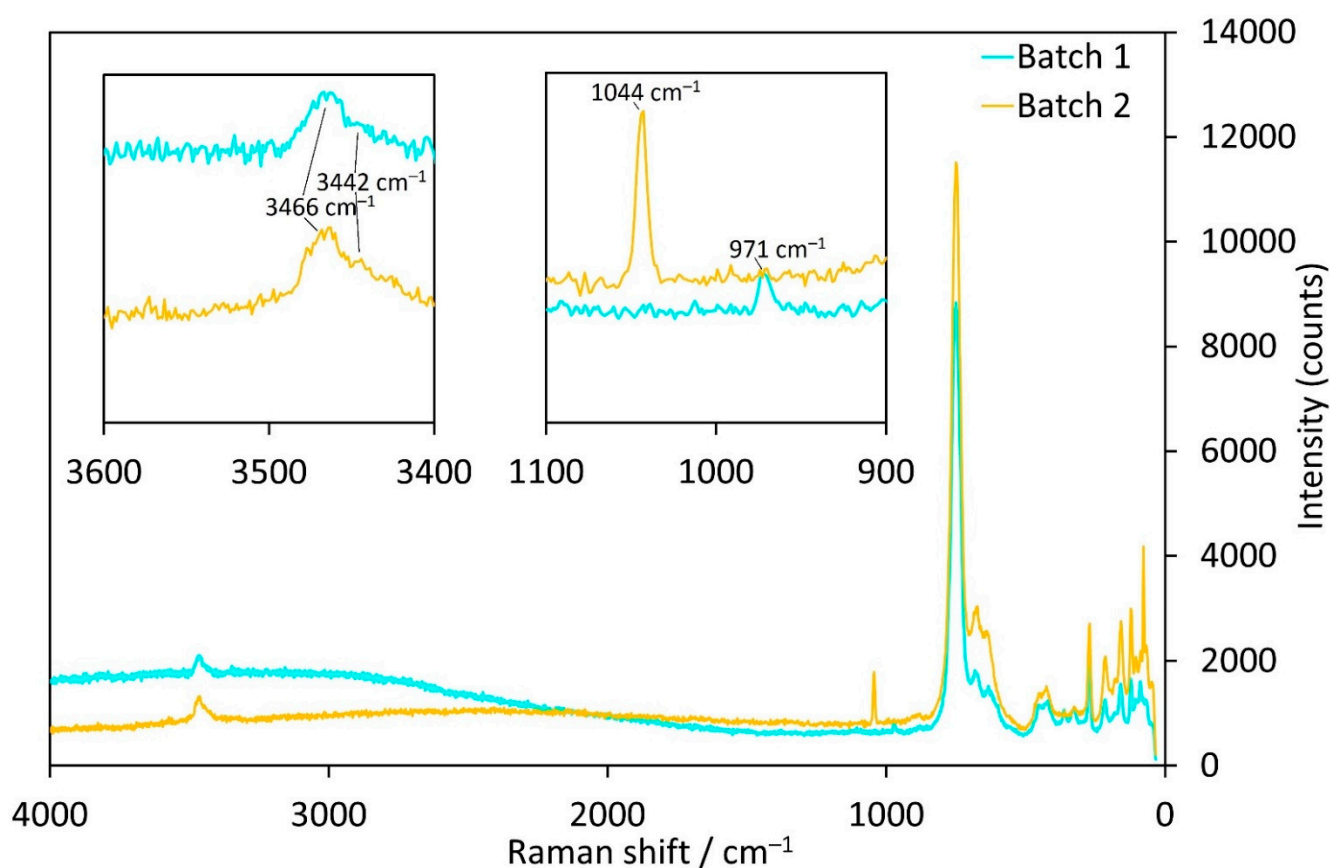


Figure 6. Raman spectra of $\text{Co}_3(\text{TeO}_3)_2(\text{OH})_2$ samples with incorporated SO_4^{2-} (batch 1, cyan) or NO_3^- ions (batch 2, orange).

The Mn-samples from batches 8 (Cl^- as counter anion) and 9 (Br^- as counter anion) have almost the same Raman spectra (Figure 7). Between 3600 and 3500 cm^{-1} , two OH-stretching vibrations are discernible with maxima around 3560 and 3515 cm^{-1} . In contrast, the corresponding OH modes are at 3466 and 3442 cm^{-1} for batches 1 and 2 above (Figure 6). No bands corresponding to a foreign anion group were observed in the 1100–900 cm^{-1} region unlike for the crystals from batches 1 and 2. However, crystals from batch 4 (with CO_3^{2-} as counter anion) show different bands in both of these characteristic ranges. The first band at 3560 cm^{-1} is distinctly weaker than for the crystals from batches 8 and 9.

Given the fact that for four of the five investigated samples the band at higher Raman shifts is more intense than the neighbouring one except for batch 4 (CO_3^{2-}), this indicates that the inclusion of CO_3^{2-} influences the signal of one type of OH^- groups in a different way than inclusion of Cl^- or Br^- . Furthermore, from the Raman spectra displayed in Figure 7, together with the results from SEM-EDS measurements of batches 8 and 9, we can assume that the channels are partially filled with both OH^- groups and a foreign anion (Cl^- , Br^- , CO_3^{2-}) in the single-crystals.

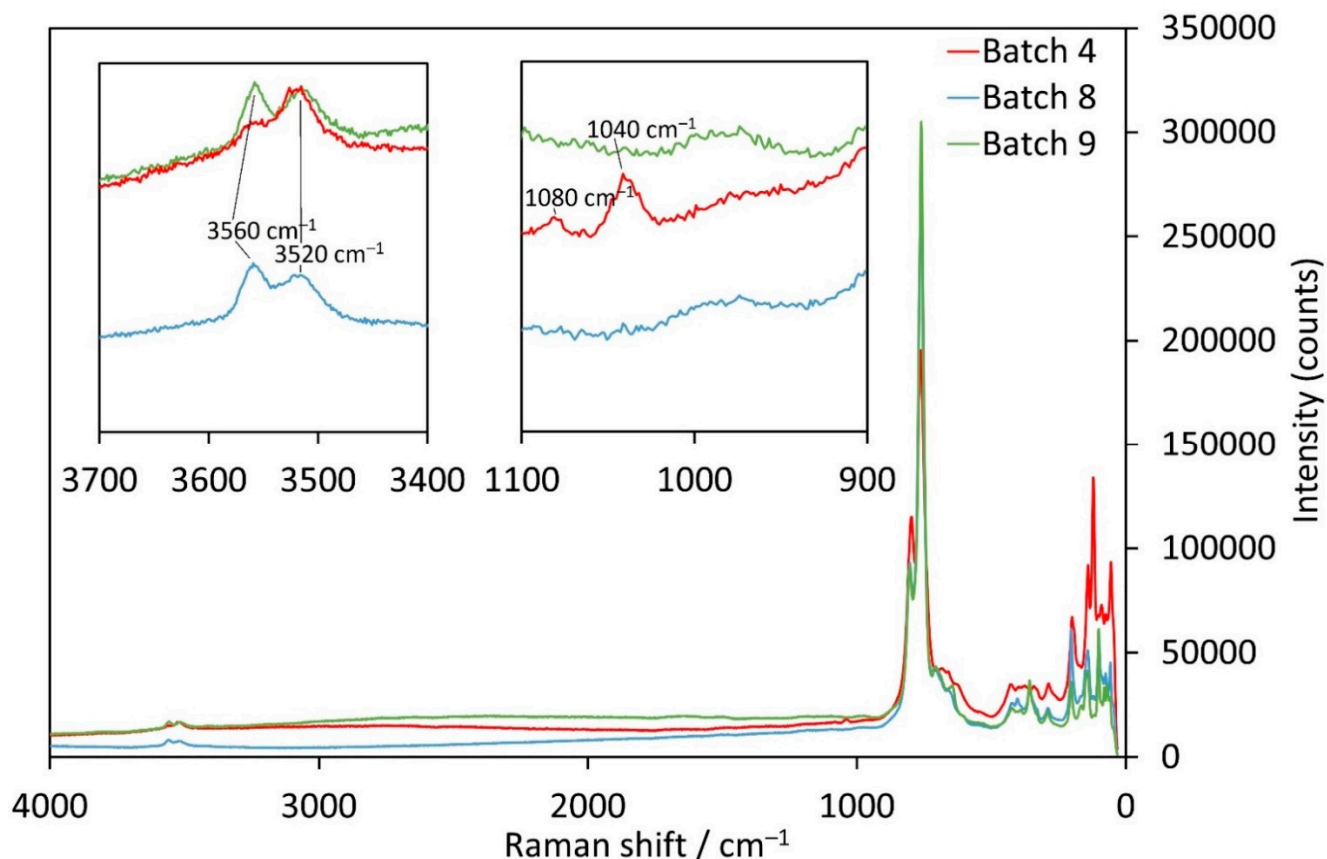


Figure 7. Raman spectra of $\text{Mn}_3(\text{TeO}_3)_2(\text{OH})_2$ samples with incorporated CO_3^{2-} (batch 4, red), Cl^- (batch 8, blue) or Br^- ions (batch 9, green).

When looking for characteristic bands originating from the CO_3^{2-} group itself, two bands between 1100 and 1000 cm^{-1} can be observed. The one with lower intensity at 1080 cm^{-1} fits perfectly with the symmetric stretch of a carbonate ion, like in Na_2CO_3 (1079 cm^{-1} [39]). On the other hand, the occurrence of the band with higher intensity at 1040 cm^{-1} is not so clear and might be caused either by the presence of a HCO_3^- group where the bands are shifted towards lower wavenumbers like in KHCO_3 (1005 cm^{-1} [39]), or to possible weak bonding interactions involving the carbonate anion itself. Possible bonding partners are either the OH^- groups inside the channels or the tellurium atoms directed towards the centre of the channel. As an interaction with the remaining hydroxide groups in the channels would most likely cause a shift of the 3560 cm^{-1} band (which is not observed), an interaction of the carbonate O atoms with the Te1 atoms is the most probable situation. It should be noted that a contamination by nitrate (the NO_3^- anion also matches the Raman shift) seems rather unlikely. The symmetrical nitrate band (crystals of batch 2) is much stronger and has a higher intensity than the one at 1040 cm^{-1} for the carbonate sample. Moreover, no reasonable contamination sources could be identified by phase analysis of the obtained bulk for the sample from batch 4.

Based on literature data for the $[\text{TeO}_3]^{2-}$ group [40] and analyses of the Raman spectra of several oxidotellurate(IV) minerals [41–43], certain bands were assigned to

the corresponding vibrational modes. A free $[\text{TeO}_3]^{2-}$ ion has C_{3v} symmetry, and four modes can be expected: $\nu_1 (A_1) = 758 \text{ cm}^{-1}$, $\nu_2 (A_1) = 364 \text{ cm}^{-1}$, $\nu_3 (E) = 703 \text{ cm}^{-1}$ and $\nu_4 (E) = 326 \text{ cm}^{-1}$ [41]. In the case of the $M_3(\text{TeO}_3)_2(\text{OH})_2$ structure type, two different, isolated $[\text{TeO}_3]^{2-}$ groups are present, corresponding to the Te1 and Te2 sites. Te2 has a site symmetry of $3m.$, which agrees with the C_{3v} symmetry of the free $[\text{TeO}_3]^{2-}$ anion and therefore only four bands should be expected. Te1 has site symmetry $.m.$, therefore the given bands could be split. Furthermore, Te2 is bonded by the three oxygen atoms at closer distances than Te1. Hence, it can be expected that each of the aforementioned four modes can lead to two vibration bands, corresponding to the two different Te sites. Finally, also the specific M atom in $M_3(\text{TeO}_3)_2(\text{OH})_2$ -type compounds has an obvious influence on the position of the $[\text{TeO}_3]^{2-}$ bands. For $M = \text{Co}$ (batches 1, 2), the mean Te–O distances are slightly larger [1.897 Å (Te1), 1.859 Å (Te2) for batch 1 and 1.895 Å (Te1), 1.859 Å (Te2) for batch 2] than for the $M = \text{Mn}$ compounds [1.880 Å (Te1), 1.847 Å (Te2) for batch 8 and 1.880 Å (Te1), 1.851(9) Å (Te2) for batch 9]. This difference exists despite the Co-compounds being measured at $-173 \text{ }^\circ\text{C}$ and the Mn-compounds at room temperature.

The Mn-samples show two bands at $804\text{--}801 \text{ cm}^{-1}$ and $762\text{--}760 \text{ cm}^{-1}$, which correspond to the $\nu_1 [\text{TeO}_3]^{2-}$ symmetric stretching mode of the Te1- and Te2-centred polyhedra, respectively. For the Co-samples, only one band is clearly visible in this range at 749 cm^{-1} , although a very weak shoulder can be seen at around 795 cm^{-1} . The bands of the Co-samples appear at lower wavenumbers, in accordance with the aforementioned difference in Te–O bond lengths. The $\nu_3 [\text{TeO}_3]^{2-}$ antisymmetric stretching mode (703 cm^{-1} for a free $[\text{TeO}_3]^{2-}$ anion) can be observed at $688\text{--}679 \text{ cm}^{-1}$ and $657\text{--}645 \text{ cm}^{-1}$ for the Mn-samples, as well as $677\text{--}675 \text{ cm}^{-1}$ and $635\text{--}629 \text{ cm}^{-1}$ for the Co-samples. It should be noted that the range of the Raman shifts varies much more than for the ν_1 modes because the corresponding bands have a much lower intensity and are rather broad.

Assigning the ν_2 and ν_4 bending modes is less straightforward, reflected also by the given literature values that are more ambiguous. Moreover, in this low-energetic spectral region vibrations of the $[\text{MO}_6]$ structural units and lattice modes occur. In most analyses of oxidotellurate(IV) minerals, the $\nu_4 (E) [\text{TeO}_3]^{2-}$ bending modes were assigned between 400 and 500 cm^{-1} rather than in the neighbourhood of the 326 cm^{-1} of the free anion. If this is assumed to be the case for $M_3(\text{TeO}_3)_2(\text{OH})_2$ -type structures as well, then the bands at $428\text{--}426 \text{ cm}^{-1}$ and $400\text{--}394 \text{ cm}^{-1}$ for the Mn-compounds, and $454\text{--}452 \text{ cm}^{-1}$ and $426\text{--}424 \text{ cm}^{-1}$ for the Co-samples could be assigned. Finally, for the $\nu_2 (A_1) [\text{TeO}_3]^{2-}$ bending modes the bands at $362\text{--}357 \text{ cm}^{-1}$ and $343\text{--}334 \text{ cm}^{-1}$ (Mn) and 326 cm^{-1} and $362\text{--}359 \text{ cm}^{-1}$ (Co) are considered as relevant.

4. Conclusions

Using complementary analytical methods (single-crystal and powder X-ray diffraction, energy-dispersive X-ray spectrometry, Raman spectroscopy), we could show that foreign anions such as Cl^- , Br^- , SO_4^{2-} , SeO_4^{2-} , CO_3^{2-} or NO_3^- can be incorporated into the crystal structure of $M^{\text{II}}_3(\text{TeO}_3)_2(\text{OH})_2$ compounds ($M = \text{Mg}, \text{Mn}, \text{Co}, \text{Ni}$), where they partly substitute OH^- anions in large hexagonal channels. The size of the incorporated foreign anion correlates with the size of the channel diameter and supports the refined structure model. Due to the large diameter of the channels, in all cases, the interaction of the disordered components in the channels with framework atoms is very weak, which causes high displacements from their ideal positions. In a more elaborated crystal-chemical scheme, the incorporation of monovalent or divalent anions or anionic groups X can be expressed by the general formula $M_3(\text{TeO}_3)_2(\text{OH})_{1.5}^{0.5+} \{(X_{x/n})(\text{OH})_{0.5-x}\}^{0.5-}$ ($0.5 \leq x \leq 0$; $n = 1, 2$) where the anionic part in curly brackets denotes the components situated in the channels.

Supplementary Materials: The following supporting information can be downloaded at: <https://www.mdpi.com/article/10.3390/cryst12101380/s1>, Table S1: Data collection and refinement details of related $M^{II}_3(\text{TeO}_3)_2(\text{OH})_2$ -type compounds; Table S2: Selected interatomic distances/Å in the crystal structures of related $M^{II}_3(\text{TeO}_3)_2(\text{OH})_2$ -type compounds; Figure S1: PXRD measurements of bulk material; Figure S2: Crystal structure of $\text{Mn}^{II}_3(\text{TeO}_3)_2(\text{OH})_{1.5}(\text{SO}_4)_{0.15}(\text{OH})_{0.20}$ with further disorder modelling of the sulfate group in the hexagonal channels.

Author Contributions: F.E.: Conceptualization; Investigation; Visualization; Data curation; Formal analysis; Writing—original draft; Writing—review and editing. M.W.: Conceptualization; Investigation; Visualization; Data curation; Resources; Supervision; Writing—original draft; Writing—review and editing. O.P.M.: Investigation; Data curation; Writing—review and editing. U.K.: Investigation; Data curation; Writing—review and editing. E.L.: Investigation; Data curation; Writing—review and editing. All authors have read and agreed to the published version of the manuscript.

Funding: Support funding was provided to OPM by an Australian Government Research Training Program (RTP) Scholarship, a Monash Graduate Excellence Scholarship (MGES) and a Monash–Museums Victoria Scholarship (Robert Blackwood).

Data Availability Statement: The data presented in this study are available in The Cambridge Crystallographic Data Centre (CCDC) and can be obtained free of charge via www.ccdc.cam.ac.uk/structures, accessed on 25 September 2022.

Acknowledgments: The X-ray Centre of TU Wien is acknowledged for providing access to the single-crystal and powder X-ray diffractometers. The authors thank Emma Ogden for help with the hydrothermal synthesis. The authors also acknowledge TU Wien Bibliothek for financial support through its Open Access Funding Programme.

Conflicts of Interest: The authors declare no conflict of interest.

References

1. Ivanov, S.A.; Nordblad, P.; Mathieu, R.; Tellgren, R.; Ritter, C.; Golubko, N.V.; Politova, E.D.; Weil, M. New type of incommensurate magnetic ordering in Mn_3TeO_6 . *Mater. Res. Bull.* **2011**, *46*, 1870–1877. [[CrossRef](#)]
2. Ivanov, S.A.; Ritter, C.; Nordblad, P.; Tellgren, R.; Weil, M.; Carolus, V.; Lottermoser, T.; Fiebig, M.; Mathieu, R. New insights into the multiferroic properties of Mn_3TeO_6 . *J. Phys. D Appl. Phys.* **2017**, *50*, 085001. [[CrossRef](#)]
3. Arévalo-López, Á.M.; Solana-Madruga, E.; Aguilar-Maldonado, C.; Ritter, C.; Mentré, O.; Atfield, J.P. Magnetic frustration in the high-pressure $\text{Mn}_2\text{MnTeO}_6$ (Mn_3TeO_6 -II) double perovskite. *Chem. Commun.* **2019**, *55*, 14470–14473. [[CrossRef](#)] [[PubMed](#)]
4. Fruchart, D.; Montmory, M.C.; Bertaut, E.F.; Bernier, J.C. Structures magnétiques de Mn_2TeO_6 et V_2WO_6 . Stabilité des modes magnétiques observés. *J. Phys.* **1980**, *41*, 141–147. [[CrossRef](#)]
5. Matsubara, N.; Damay, F.; Vertruyen, B.; Barrier, N.; Lebedev, O.I.; Boullay, P.; Elkaim, E.; Manuel, P.; Khalyavin, D.D.; Martin, C. Mn_2TeO_6 : A Distorted Inverse Trirutile Structure. *Inorg. Chem.* **2017**, *56*, 9742–9753. [[CrossRef](#)]
6. Trömel, M.; Schmid, D. Tellurite des zweiwertigen Mangans, Kobalts und Nickels. *Z. Anorg. Allg. Chem.* **1972**, *387*, 230–240. [[CrossRef](#)]
7. Trömel, M.; Scheller, T. Die Kristallstruktur von $\text{Co}_6\text{Te}_5\text{O}_{16}$. *Z. Anorg. Allg. Chem.* **1976**, *427*, 229–234. [[CrossRef](#)]
8. Miletich, R. Copper-substituted manganese-denningites, $\text{Mn}(\text{Mn}_{1-x}\text{Cu}_x)(\text{Te}_2\text{O}_5)_2$ ($0 \leq x \leq 1$): Synthesis and crystal chemistry. *Mineral. Petrol.* **1993**, *48*, 129–145. [[CrossRef](#)]
9. Cooper, M.A.; Hawthorne, F.C. The crystal structure of spiroffite. *Can. Mineral.* **1996**, *34*, 821–826.
10. Irvine, J.T.S.; Johnston, M.G.; Harrison, W.T.A. Lone-pair containment in closed cavities. The $\text{MTe}_6\text{O}_{13}$ ($M = \text{Mn, Ni, Co}$) family of ternary oxides. *Dalton Trans.* **2003**, *13*, 2641–2645. [[CrossRef](#)]
11. Feger, C.R.; Schimek, G.L.; Kolis, J.W. Hydrothermal synthesis and characterization of $\text{M}_2\text{Te}_3\text{O}_8$ ($M = \text{Mn, Co, Ni, Cu, Zn}$): A series of compounds with the spiroffite structure. *J. Solid State Chem.* **1999**, *143*, 246–253. [[CrossRef](#)]
12. Kohn, K.; Akimoto, S.-I.; Uesu, Y.; Asai, K. Crystal Structure and Magnetic Properties of MnTeO_3 , CoTeO_3 and NiTeO_3 . *J. Phys. Soc. Jpn.* **1974**, *37*, 1169. [[CrossRef](#)]
13. Kohn, K.; Inoue, K.; Horie, O.; Akimoto, S.-I. Crystal chemistry of MSeO_3 and MTeO_3 ($M = \text{Mg, Mn, Co, Ni, Cu, and Zn}$). *J. Solid State Chem.* **1976**, *18*, 27–37. [[CrossRef](#)]
14. Eder, F.; Weil, M. Phase formation studies and crystal structure refinements in the $\text{Mn}^{II}/\text{Te}^{IV}/\text{O}/(\text{H})$ system. *Z. Anorg. Allg. Chem.* **2022**. [[CrossRef](#)]
15. Ptáček, P. Substituents and Dopants in the Structure of Apatite. In *Apatites and Their Synthetic Analogues*; IntechOpen: London, UK, 2016; pp. 289–334.
16. Peacor, D.R.; Sarp, H.; Dunn, P.J.; Innes, J.; Nelen, J.A. Defernite from the Kombat mine, Namibia: A second occurrence, structure refinement, and crystal chemistry. *Am. Mineral.* **2006**, *73*, 888–893.
17. Degen, T.; Sadki, M.; Bron, E.; König, U.; Nénert, G. The HighScore suite. *Powder Diffr.* **2014**, *29*, S13–S18. [[CrossRef](#)]

18. APEX3 and SAINT; Bruker AXS Inc.: Madison, WI, USA, 2016.
19. Krause, L.; Herbst-Irmer, R.; Sheldrick, G.M.; Stalke, D. Comparison of silver and molybdenum microfocus X-ray sources for single-crystal structure determination. *J. Appl. Cryst.* **2015**, *48*, 3–10. [[CrossRef](#)]
20. Sheldrick, G.M. SHELXT—Integrated space-group and crystal-structure determination. *Acta Crystallogr.* **2015**, *71*, 3–8. [[CrossRef](#)]
21. Sheldrick, G.M. Crystal structure refinement with SHELXL. *Acta Crystallogr.* **2015**, *71*, 3–8.
22. ATOMS for Windows; Shape Software: Kingsport, TN, USA, 2006.
23. Perez, G.; Lasserre, F.; Moret, J.; Maurin, M. Structure cristalline des hydroxytellurites de nickel et de cobalt. *J. Solid State Chem.* **1976**, *17*, 143–149. [[CrossRef](#)]
24. Parsons, S.; Flack, H.D.; Wagner, T. Use of intensity quotients and differences in absolute structure refinement. *Acta Crystallogr.* **2013**, *69*, 249–259. [[CrossRef](#)] [[PubMed](#)]
25. Flack, H.D. On enantiomorph-polarity estimation. *Acta Crystallogr.* **1983**, *39*, 876–881. [[CrossRef](#)]
26. Wojdyr, M. Fityk: A general-purpose peak fitting program. *J. Appl. Crystallogr.* **2010**, *43*, 1126–1128. [[CrossRef](#)]
27. Shirkhanlou, M.; Weil, M. The Mg member of the isotopic series $M\text{Te}_6\text{O}_{13}$. *Acta Crystallogr.* **2013**, *69*, i18.
28. Poupon, M.; Barrier, N.; Pautrat, A.; Petit, S.; Perez, O.; Bazin, P. Investigation of $\text{Co}_6(\text{OH})_3(\text{TeO}_3)_4(\text{OH})\cdot 0.9(\text{H}_2\text{O})$: Synthesis, crystal and magnetic structures, magnetic and dielectric properties. *J. Solid State Chem.* **2019**, *270*, 147–155. [[CrossRef](#)]
29. Christy, A.G.; Mills, S.J.; Kampf, A.R. A review of the structural architecture of tellurium oxycompounds. *Mineral. Mag.* **2016**, *80*, 415–545. [[CrossRef](#)]
30. Gagné, O.C.; Hawthorn, F.C. Bond-length distributions for ions bonded to oxygen: Alkali and alkaline-earth metals. *Acta Crystallogr.* **2016**, *72*, 602–625. [[CrossRef](#)]
31. Gagné, O.C.; Hawthorn, F.C. Bond-length distributions for ions bonded to oxygen: Results for the transition metals and quantification of the factors underlying bond-length variation in inorganic solids. *IUCr* **2020**, *7*, 581–629. [[CrossRef](#)]
32. Shannon, R.D. Revised effective ionic radii and systematic studies of interatomic distances in halides and chalcogenides. *Acta Crystallogr.* **1976**, *32*, 751–767. [[CrossRef](#)]
33. Gilli, G.; Gilli, P. *The Nature of the Hydrogen Bond: Outline of a Comprehensive Hydrogen Bond Theory*; Oxford University Press: New York, NY, USA, 2009.
34. Galy, J.; Meunier, G.; Andersson, S.; Åström, A. Stéréochimie des éléments comportant des paires non liées: Ge(II), As(III), Se(IV), Br(V), Sn(II), Sb(III), Te(IV), I(V), Xe(VI), Tl(I), Pb(II), et Bi(III) (oxydes, fluorures et oxyfluorures). *J. Solid State Chem.* **1975**, *13*, 142–159. [[CrossRef](#)]
35. Stöger, B.; Weil, M.; Silich, K.A.; Olenev, A.V.; Berdonosov, P.S.; Dolgikh, V.A. Synthesis and Structural Characterization of New Phases in the Cubic $M_3\text{Te}_2\text{O}_6X_2$ ($M = \text{Sr}, \text{Ba}$; $X = \text{Cl}, \text{Br}$) Structure Family. *Z. Anorg. Allg. Chem.* **2011**, *637*, 1322–1329. [[CrossRef](#)]
36. Amoros, P.; Marcos, M.D.; Roca, M.; Beltran-Porter, A.; Beltran Porter, D. Synthetic Pathways for New Tubular Transition Metal Hydroxo and Fluoro-Selenites: Crystal Structures of $M_{12}(X)_2(\text{SeO}_3)_8(\text{OH})_6$ ($M = \text{Co}^{2+}, \text{Ni}^{2+}$; $X = (\text{OH})^-$). *J. Solid State Chem.* **1996**, *126*, 169–176. [[CrossRef](#)]
37. Jenkins, H.D.B.; Thakur, K.P. Reappraisal of thermochemical radii for complex ions. *J. Chem. Educ.* **1979**, *56*, 576–577. [[CrossRef](#)]
38. Nicholls, P. Introduction: The biology of the water molecule. *CMLS Cell. Mol. Life Sci.* **2000**, *57*, 987–992. [[CrossRef](#)] [[PubMed](#)]
39. Weidlein, J.; Müller, U.; Dehnicke, K. *Schwingungsfrequenzen I (Hauptgruppenelemente)*; Georg Thieme Verlag: Stuttgart, Germany, 1981.
40. Farmer, V.C. (Ed.) *Mineralogical Society Monograph 4: The Infrared Spectra of Minerals*; The Mineralogical Society: London, UK, 1974.
41. Frost, R.L.; Keeffe, E.C. Raman spectroscopic study of the tellurite minerals: Graemite $\text{CuTeO}_3\cdot\text{H}_2\text{O}$ and teineite $\text{CuTeO}_3\cdot 2\text{H}_2\text{O}$. *J. Raman Spectrosc.* **2009**, *40*, 128–132. [[CrossRef](#)]
42. Frost, R.L.; Keeffe, E.C. Raman spectroscopic study of the tellurite mineral: Sonoraite $\text{Fe}^{3+}\text{Te}^{4+}\text{O}_3(\text{OH})\cdot\text{H}_2\text{O}$. *J. Raman Spectrosc.* **2009**, *40*, 133–136. [[CrossRef](#)]
43. Rumsey, M.S.; Welch, M.D.; Mo, F.; Kleppe, A.K.; Spratt, J.; Kampf, A.R.; Raanes, M.P. Millsite $\text{CuTeO}_3\cdot 2\text{H}_2\text{O}$: A new polymorph of teineite from Gråurdjfellet, Oppdal kommune, Norway. *Mineral. Mag.* **2018**, *82*, 433–444. [[CrossRef](#)]